

Effect of the growth orientation on the physical properties of $\text{Sr}_2\text{CoNbO}_6$ thin films

Ajay Kumar,¹ Ramcharan Meena,^{1,2} M. Miryala,³ K. Ueno,³ and Rajendra S. Dhaka^{1,*}

¹*Department of Physics, Indian Institute of Technology Delhi, Hauz Khas, New Delhi-110016, India*

²*Material Science Division, Inter-University Accelerator Center, Aruna Asaf Ali Road, New Delhi-110067, India*

³*Shibaura Institute of Technology, 3-7-5 Toyosu campus, Koto-ku, Tokyo 135-8548, Japan*

(Dated: June 13, 2023)

We study the effect of the growth orientation on the structural, electronic, and hence transport properties of $\text{Sr}_2\text{CoNbO}_6$ thin films grown on the orthorhombic NGO(100) and cubic MgO(100) substrates. The x-ray diffraction patterns show the growth of the thin film along a -axis resulting in the asymmetric ($b \neq c$) in-plane compressive strain in case of NGO(100), whereas along c -axis with tensile strain in case of MgO(100) substrate. The temperature dependent resistivity measurements indicate the lower electronic conductivity for the film grown on the NGO(100) substrate, which is found to be correlated with the higher degree of the oxygen deficiencies and hence larger concentration of the insulating Co^{2+} in this sample. Further, the x-ray photoemission spectroscopy measurements show that Sr and Nb are present in the 2+ and 4+ valence state, whereas Co exist in the 2+, 3+ as well as 4+ states, fraction of which was found to vary with the growth orientation. Moreover, the analysis of leakage current using the sum exponent model indicate the presence of two different relaxation mechanisms in these samples.

I. INTRODUCTION

A stable crystal structure and hence possibility to accommodate the wide range of the elements in the perovskite structure (ABO_3 ; A: rare earth/ alkali earth metals, B: transition metals) give rise to the exotic physical properties such as giant magnetoresistance, spin frustration, multiferroicity, etc.[1–5], resulting their important technological applications in resistive switching devices, magnetocaloric effect, solid oxide fuel cells, photovoltaics, etc. [6–9]. Several external perturbations like temperature, mechanical pressure, chemical pressure (doping) have been extensively used to systematically tune these properties [10–12]; however, a fine control on the oxygen stoichiometry, which govern most of their physical properties, is still a major challenge in the family of complex oxides [13, 14]. In this regard, substrate induced strain in the epitaxial thin films has become novel tool to engineer the oxygen concentration, and resulting electronic structure and magnetic properties of these samples [15–19]. Also, the single crystalline oxide substrates with different lattice parameters can give the flexibility to tailor the oxygen content for the desired physical properties [20, 21]. Moreover, the double perovskite oxides with the general formula $\text{A}_2\text{BB}'\text{O}_6$ have further attracted the research community, where the degree of rock salt like ordering in the BO_6 and $\text{B}'\text{O}_6$ octahedra has been widely used to engineer their physical properties [22–24]. The recent neutron powder diffraction and the x-ray absorption spectroscopy (XAS) measurements on the La substituted $\text{Sr}_{2-x}\text{La}_x\text{CoNbO}_6$ samples demonstrate that the degree of octahedral distortion plays a key role in controlling the magnetic and electronic properties of these samples [25, 26]. Interestingly, the substrate

induced strain in the thin film samples can significantly rotate/ tilt the $(\text{B}/\text{B}')\text{O}_6$ octahedra by manipulating the $\text{B}/\text{B}'\text{-O}$ bond length and/or $\text{B}/\text{B}'\text{-O-B}/\text{B}'$ bond angles [16, 27, 28]. For example, Kleibecker *et al.* proposed an interesting approach of growing the ordered thin films from the disordered bulk double perovskite target materials, where the formation of the B-site cages of two different volume has been observed, resulting from the tilting of the two adjacent $(\text{B}/\text{B}')\text{O}_6$ octahedra towards in-plane and out-of plane directions of the (111) oriented substrate, respectively [29].

More importantly, the epitaxial thin films of the Co-based perovskite oxides are of particular interest due to the various possible valence and spin-states of Co, which can be easily altered by changing the crystal field splitting with the help of the misfit induced strain in the epitaxial thin films [16, 30–32]. Chen *et al.* reported that a mechanical pressure of 40 GPa on $\text{SrCo}_{0.5}\text{Ru}_{0.5}\text{O}_{3-\delta}$ sample can completely transforms the Co^{3+} ions from high spin (HS) to low spin (LS) state due to reduction in the Co–O bond distance [10]. This suggest that the substrate induced strain can be used as an alternative tool to manipulate the electronic structure of such compounds in the epitaxial thin films. For example, even a small degree of the compressive strain in the $\text{La}_2\text{CoMnO}_6$ thin films (grown on LSAT and LaAlO_3 substrates) favors the in-plane magnetic anisotropy, whereas a tensile strain (on SrTiO_3 substrate) results in the out-of-plane magnetic anisotropy due to difference in the cell parameter in the two cases [30]. In this line, $\text{Sr}_2\text{CoNbO}_6$ due to its moderate charge and ionic radii difference between two B-site atoms (Co^{3+} and Nb^{5+}), which is crucial for achieving the B-site ordering [33, 34], results in the intriguing physical properties like colossal dielectric response and complex ac impedance spectroscopy [35–37]. Recently, we have extensively studied the magnetic, transport, and electronic properties of La substituted $\text{Sr}_{2-x}\text{La}_x\text{CoNbO}_6$ bulk samples, which shows the low

* rsdhaka@physics.iitd.ac.in

temperature cluster-glass-like behavior for $\text{Sr}_2\text{CoNbO}_6$ and insulating/semiconducting nature with the electronic activation energy of 0.27 eV [38, 39]. Also, Wang *et al.* reported the colossal dielectric properties in $\text{Sr}_2\text{CoNbO}_6$ and its strong correlation with the conductivity of the sample [36]. Theoretical calculations by He *et al.* claim the $\text{Sr}_2\text{CoNbO}_6$ as an indirect band gap semiconductor with a band gap of 2.926 eV [40]. In order to tune the electronic band structure in a controlled manner, the epitaxial thin films of $\text{Sr}_2\text{CoNbO}_6$ were grown on different substrates with the varying degree as well as the direction of the substrate induced strain, where the compressive and tensile strains were found to decrease and increase the electronic band gap, respectively [20]. The analysis suggests that the cumulative effect of the substrate induced strain, oxygen non-stoichiometry, and degree of covalency character in the bonding govern the underlined transport mechanism in the compound [20]. Thus, a precise understanding of its electronic structure is necessary for the device fabrication. However, the effect of growth orientation of the films on the electronic structure has not been studied, which can be useful to disentangle the contribution of various factors on the electronic structure of $\text{Sr}_2\text{CoNbO}_6$. Moreover, an estimation of the steady-state leakage current is also crucial for its possible use in the energy storage devices, dynamic random access memory (DRAM), transistors etc. [41–43].

Therefore, we investigate the epitaxial thin films of $\text{Sr}_2\text{CoNbO}_6$ on orthorhombic NGO(100) substrate with the asymmetric in-plane compressive strain and cubic MgO(100) substrate with the symmetric tensile strain. The out-of-plane x-ray diffraction (XRD) measurements reveal the growth of the thin films along a and c -axis on the NGO(100) and MgO(100) substrates. A periodic pattern in the surface topography is observed with the average roughness of around 4 nm for both the films using atomic force microscopy. The temperature dependent resistivity shows the lower electronic conductivity in case of film grown on the NGO(100) substrate, which is supported by the higher activation energy and lower effective density of states near the Fermi level as compared to that on MgO(100) substrate. The x-ray photoemission measurements clearly show the higher oxygen deficiencies and resulting larger fraction of the Co in 2+ valence state in case of the film on NGO(100) substrate, causing its lower electronic conductivity. Further, the possible mechanisms governing the leakage current in the film on NGO(100) substrate, using the dc step voltage, has been discussed to understand its possible use in the charge storage devices.

II. EXPERIMENTAL

The details about the sample preparation and the physical properties of the bulk $\text{Sr}_2\text{CoNbO}_6$ target sample can be found in Refs. [26, 38, 39]. The thin films of 70 ± 5 nm were grown from the bulk target material us-

ing the pulsed laser deposition (PLD) technique [32] on $\text{NdGaO}_3(\text{NGO})(100)$ and $\text{MgO}(100)$ substrates. In order to optimize the thickness of the films, we first deposited a film on Si(100) by partially shadowing the substrate to make a sharp step and estimated the film thickness using a stylus profiler across the step. We then used the same deposition parameters for both the films, which were grown at 800°C temperature and 10^{-3} mbar oxygen partial pressure using $1.5\text{--}2$ J cm^{-2} laser fluence and 5Hz repetition rate. A post-growth annealing for 15 minutes was performed at 50 mbar oxygen pressure for both the samples at the deposition temperature.

We carried out the XRD measurements in the Bragg-Brentano geometry using PANalytical X'Pert³ diffractometer. The atomic force microscope (AFM) was used in the non-contact mode to study the surface topography of the films. The low temperature resistivity measurements were performed using physical property measurement system (PPMS) of Quantum design, USA, with the four probe contact method using $0.1 \mu\text{A}$ excitation current. The I-V and leakage current measurements were performed in somewhat unconventional two probe configuration on top of the films using the 2612B source meter and 6517B electrometer from Keithley. The x-ray photoemission spectroscopy (XPS) measurements were done with the monochromatic Al-K α ($h\nu = 1486.6$ eV) x-ray source. Due to the insulating nature of both the samples, a charge neutralizer was used during the measurements. Each spectrum is calibrated *w.r.t.* the offset in C 1s peak from 284.6 eV and then fitted with the mixed Lorentzian and Gaussian peak shape after subtracting the inelastic Tougaard background. We use Renishaw inVia confocal microscope with 514.5 nm laser source and 1 mW laser power to perform unpolarized Raman spectroscopy measurements.

III. RESULTS AND DISCUSSION

The orthorhombic crystal structure of NGO substrate with all the three different lattice axes ($a_{\text{NGO}}=5.433$ Å, $b_{\text{NGO}}=5.503$ Å, $c_{\text{NGO}}=7.716$ Å) results in the several possible growth orientations with varying degree of the asymmetric in-plane lattice mismatch on the different surface planes [44, 45]. In the present case, $\text{Sr}_2\text{CoNbO}_6$ with the tetragonal structure ($a_{\text{S}_2\text{CN}}=b_{\text{S}_2\text{CN}}=5.602$ Å and $c_{\text{S}_2\text{CN}}=7.921$ Å [38]) can be epitaxially grown on the NGO(100) substrate, such that b and c -axis lies in-plane of the substrate and a -axis in the out-of-plane direction. This produces an asymmetric in-plane lattice misfit $[(b_{\text{NGO}}-b_{\text{S}_2\text{CN}})/b_{\text{S}_2\text{CN}}]$ of -1.77% and -2.59% along the b and c -axis, respectively. The presence of asymmetric in-plane strain in the $\text{Sr}_2\text{CoNbO}_6$ film grown on NGO(100) substrate is schematically illustrated in Fig. 1(a). The longer out-of-plane lattice parameter of $\text{Sr}_2\text{CoNbO}_6$ as compared to NGO(100) substrate results in its corresponding peak at lower 2θ value in the XRD measurements, as shown in Fig. 1(b). The calculated out-of-

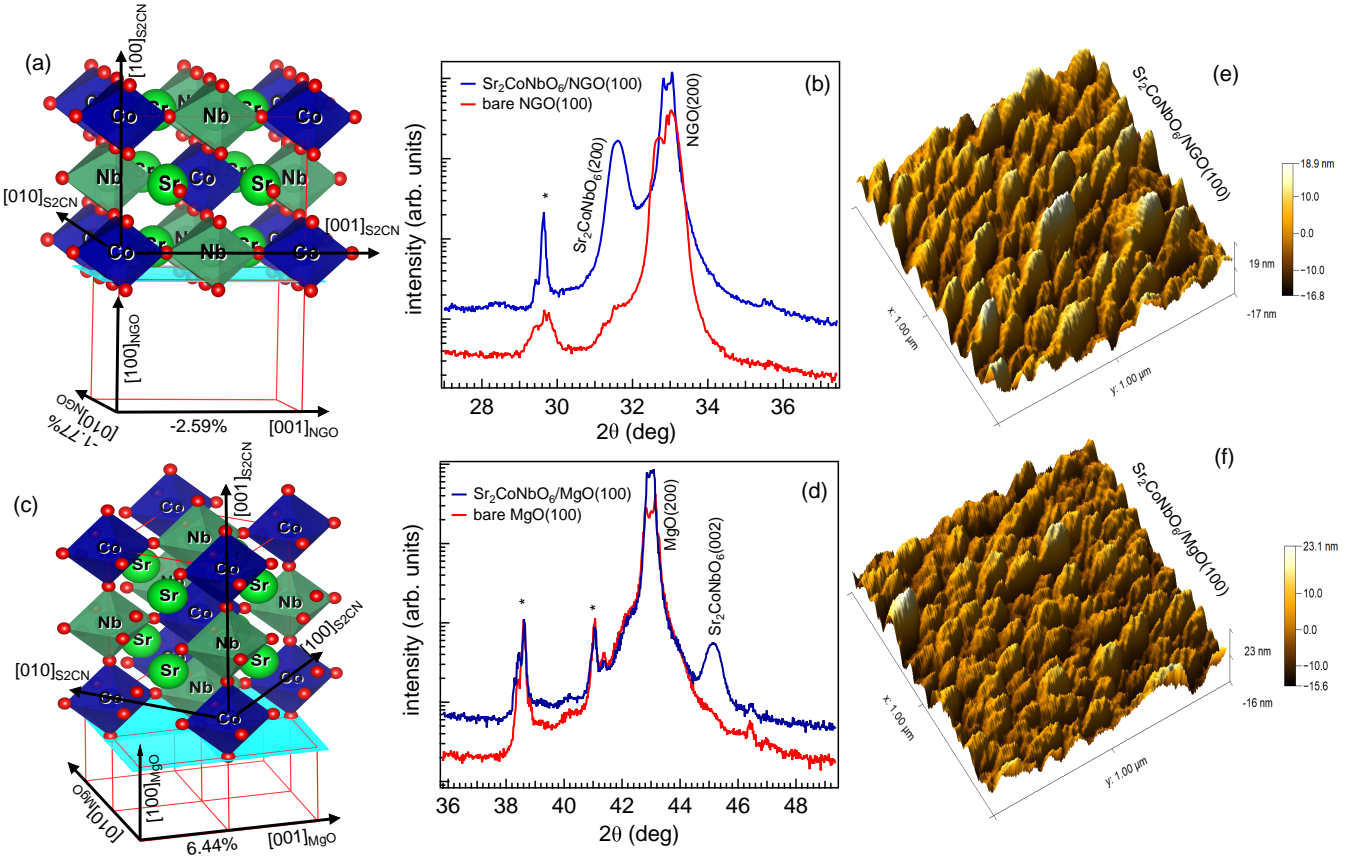


FIG. 1. (a) Schematic illustration of the growth orientation of the $\text{Sr}_2\text{CoNbO}_6$ (S2CN) thin films deposited on NGO(100) and (c) MgO(100) substrates. (b) Room temperature θ - 2θ x-ray diffraction pattern of $\text{Sr}_2\text{CoNbO}_6$ thin films grown on NGO [around (200) reflection] and (d) MgO [around (002) reflection] substrates. The asterisk symbols indicate the peaks originating from the substrates. (e) $(1 \times 1) \mu\text{m}$ AFM images of the same films grown on NGO(100) and (f) MgO(100) substrates.

plane (a -axis) lattice parameter of $\text{Sr}_2\text{CoNbO}_6$ from the XRD data is found to be 5.656 \AA , which is 0.96% longer than the bulk lattice parameter (5.602 \AA), indicating the significant effect of the in-plane compressive strain on the lattice structure of $\text{Sr}_2\text{CoNbO}_6$, which results in the change in orbital hybridization, and consequently the electronic and transport properties in the thin films, discussed later. Also, the presence of oxygen deficiencies in the perovskite thin films are also widely known to expand the unit cell [46, 47] and hence a cumulative effect of both substrate induced strain and oxygen vacancies (discussed below) are expected to govern the lattice parameter in the present case. The peak marked by asterisk symbol in Fig. 1(b) results from the crystal imperfection in the substrate, as evident from the XRD pattern of the bare NGO(100) substrate.

Further, the epitaxial growth of $\text{Sr}_2\text{CoNbO}_6$ on the cubic MgO(100) substrate ($a_{\text{MgO}} = 4.216 \text{ \AA}$) is illustrated in Fig. 1(c), where a and b -axis lie in-plane of the substrate and c -axis along the out-of-plane direction. The in-plane lattice parameters of $\text{Sr}_2\text{CoNbO}_6$ in the pseudocubic representation are $a/\sqrt{2} = 3.961 \text{ \AA}$, which results in a large lattice misfit of 6.44% with the MgO(100) substrate pro-

ducing tensile strain. This relatively large in-plane lattice misfit may also lead in the gradual relaxation in the film as we move away from the interface and reciprocal space mapping (RSM) measurements can be further helpful to directly probe the strain state in these films [48]. The presence of the film peak at the higher 2θ value in the XRD pattern as compared to the substrate, as shown in Fig. 1(d), indicate the smaller out-of-plane pseudocubic lattice parameter (in the present case, $c_{\text{pc}} = c/2$, where subscript pc represent the pseudocubic). It is important to note here that the out-of-plane lattice parameter of $\text{Sr}_2\text{CoNbO}_6$ film grown on MgO(100) substrate found to be 4.006 \AA , which is 3.8% larger than that of bulk sample in spite of the tensile in-plane strain in the film. This indicate the dominant role of oxygen vacancies in the anisotropic expansion of the unit cell of film grown on the MgO(100) substrate [47]. Further, the AFM images for both the samples are recorded to study their surface topography, as shows in Figs. 1(e) and (f) for the films grown on NGO(100) and MgO(100) substrates, respectively. The periodic patterns are observed on the surface of both the samples in $(1 \times 1) \mu\text{m}$ scan areas. However, these features are more clearly visible in case of the

film grown on NGO(100), possibly due to the relatively smaller lattice misfit of the film with the substrate as compared to the MgO(100) substrate [20]. The calculated average roughness of the films are 4.3 nm in case of NGO(100) and 3.9 nm in case of MgO(100) substrate, which is slightly higher considering the epitaxial growth. The post-growth annealing of the films in the higher oxygen partial pressure may be the possible reason for this large surface roughness.

It has been well established that the degree and direction of the lattice strain is strongly related to the presence of oxygen non-stoichiometry in the epitaxial thin films of the oxide materials due to change in the molar volume [17–19]. Further, the presence of compressive and tensile substrate induced in-plane lattice strain are known to respectively strengthen and weaken the $p-d$ orbital hybridization between the oxygen and transition metal atoms, resulting in the enhancement and reduction of the electronic conductivity in the two cases, respectively [20, 49]. Thus, in order to probe the effect of growth orientation and asymmetric in-plane strain on the electronic band structure of $\text{Sr}_2\text{CoNbO}_6$, we record the temperature dependent resistivity of both the films from 185–380 K, as shown in Fig. 2(a). We observe semiconducting/ insulating behavior in the measured temperature range for both the films. It is interesting to note that the film grown on the MgO(100) substrate shows the higher electronic conductivity as compared to that on the NGO(100) substrate, despite the compressive in-plane strain in the latter. This suggest that the effect of growth orientation of the films on their electronic structure is more prominent as compared to strain induced change in the metal-ligand orbital hybridization.

In order to understand the electronic transport mechanism in the films, the resistivity curves were modeled with the Arrhenius equation, described as

$$\rho(T) = \rho(0)\exp(E_a/k_B T), \quad (1)$$

where E_a is the activation energy require for the conduction of the charge carriers and $\rho(0)$ is the pre-exponential factor. The linear fitting of the $\ln(\rho)$ versus $1/T$ plots from 284–380K gives activation energies of 196 meV and 190 meV for the films deposited on NGO(100) and MgO(100) substrates, as shown in Figs. 2(b) and (c), respectively. This indicate the higher conductivity of the film grown on the MgO(100) substrate, as also evident from the Fig. 2(a). However, the conduction behavior of the films deviates from the Arrhenius model at the low temperatures, as shown by the green dashed lines in Figs. 2(b) and (c). We find that the conduction mechanism of the films in the low temperature region follow the variable range hopping (VRH) model of the localized charge carriers, given as

$$\rho(T) = \rho(0)\exp(T_0/T)^{1/4}, \quad (2)$$

where T_0 is the characteristic temperature defined as, $T_0 = 18/k_B N(E_F)L^3$, where $N(E_F)$ is the localized density of states (DOS) near the Fermi level and L is the

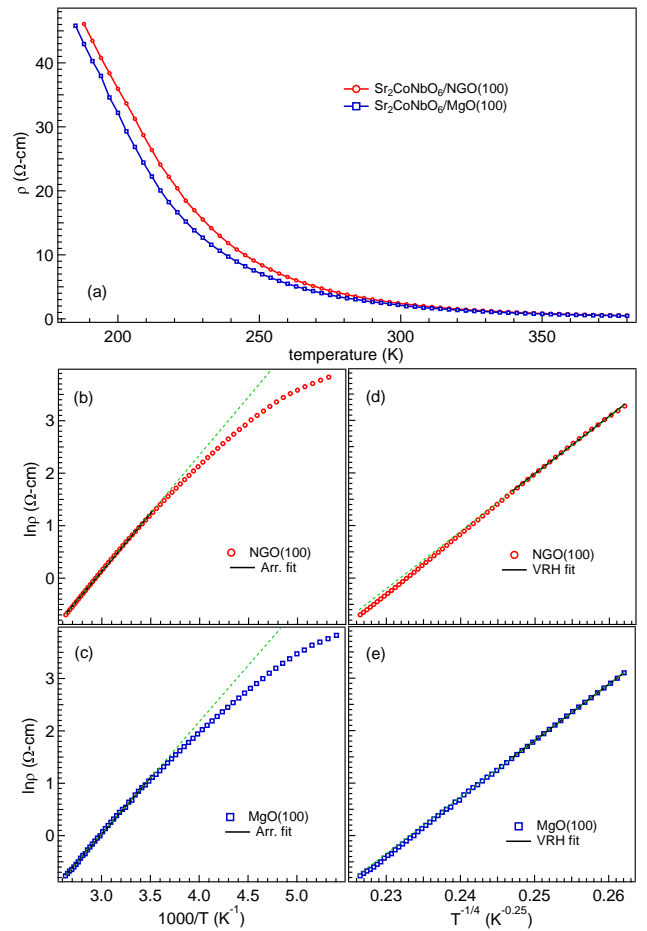


FIG. 2. (a) The temperature dependent resistivity of $\text{Sr}_2\text{CoNbO}_6$ films grown on NGO(100) and MgO(100) substrates. (b, c) The Arrhenius fitting of the high temperature resistivity data, and (g, h) the VRH fitting in the low temperature regime, for the films grown on NGO(100) and MgO(100) substrates, respectively. Here, the green dashed lines represent the deviation from the Arrhenius and VRH models in the lower and higher temperature regimes, respectively.

hopping length of the charge carriers. The slope of the $\ln(\rho)$ versus $T^{-1/4}$ curves in the low temperature region gives the value of T_0 , as shown by black solid lines in Figs. 2(d) and (e) for both the films grown on the NGO(100) and MgO(100) substrates, respectively. The estimated values of the effective DOS near the Fermi level are 17.9×10^{19} and $18.9 \times 10^{19} \text{ eV}^{-1}\text{cm}^{-3}$ for the films on NGO(100) and MgO(100) substrates, respectively, where we assume $\text{Co-O} \approx 2\text{\AA}$ as the localization length of the charge carriers. The low DOS value near the Fermi level and higher activation energy required by the charge carriers to take part in the conduction mechanism in case of the film deposited on the NGO(100) substrate results in its lower electronic conductivity as compared to the film deposited on the MgO(100) substrate. A similar reduction in the electronic conductivity of anisotropically strained $\text{La}_{0.67}\text{Ca}_{0.33}\text{MnO}_3$ films grown on

NGO(100) and NGO(001) substrates has been attributed to the rotation/tilting and distortion in the MnO_6 octahedra, as compared to the unstrained (bulk like) film on NGO(110) substrate [45]. A higher degree of distortion in the $(\text{Co}/\text{Nb})\text{O}_6$ octahedra in case of NGO(100) substrate due to the anisotropic in-plane strain can also be the possible reason for this observed reduction in the electronic conduction in the film grown on NGO(100) substrate.

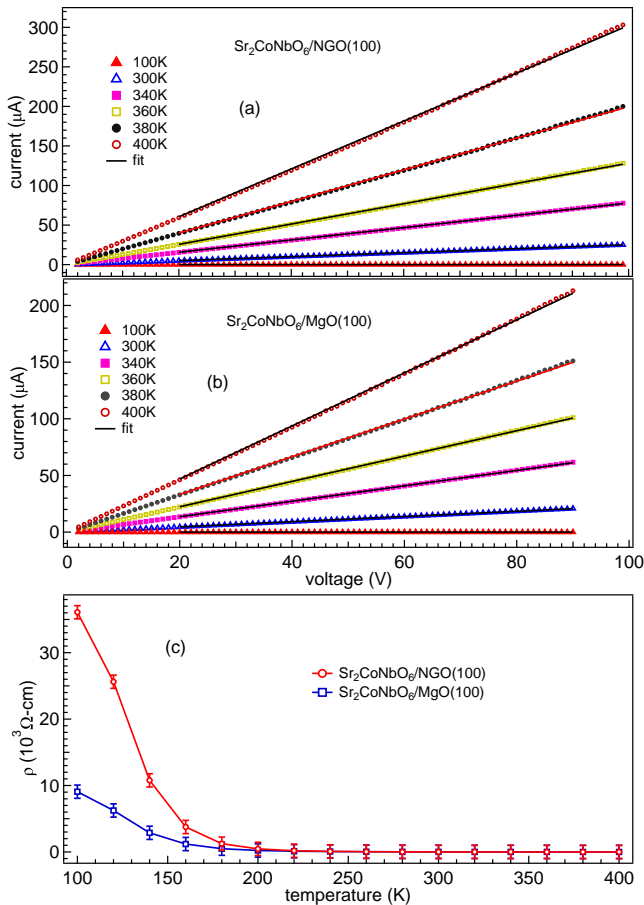


FIG. 3. The I-V data of the films grown on (a) NGO(100) and (b) MgO(100) substrates at the selected temperatures. (c) The temperature dependent resistivity curves extracted from the slope of I-V curves in the higher voltage regime, as shown by the solid black lines in (a) and (b).

In order to further quantify this effect, the temperature dependent current (I)-voltage (V) measurements are performed and the data are shown in Figs. 3(a, b) for the films grown on NGO(100) and MgO(100) substrates, respectively. The I-V curves show the linear behavior, particularly in the high voltage region and the slope of linear fit [shown by the solid lines in Figs. 3(a, b)] is used to calculate the conductance and hence resistivity of the samples as a function of temperature, as presented in Fig. 3(c). The observed higher resistivity of the film grown on the NGO(100) substrate as compared to that on MgO(100) in I-V data is consistent with the above ρ -T data, measured at the fixed excitation current.

To understand this observed change in the conduction mechanism, the x-ray photoelectron spectroscopy (XPS) measurements are performed on these samples [50, 51]. Figs. 4(a, b) show the XPS survey spectra of $\text{Sr}_2\text{CoNbO}_6$ films grown on NGO(100) and MgO(100) substrates, respectively where all the prominent peaks in the spectra are assigned to the binding energies (BEs) of the constituent elements of the target material, discarding the possibility of any elemental impurity in both the samples. Figs. 4(c, d) represent the Sr $3d$ core level spectra of these samples, which show a separation of 1.7 eV between $3d_{3/2}$ and $3d_{5/2}$ components resulting from the spin-orbit coupling. The peak position of these components (Sr $3d_{5/2}$ at 132.5 eV and Sr $3d_{3/2}$ at 134.3 eV) indicate the presence of Sr in 2+ valence state in both the samples [50, 52]. Further, the recorded Nb $3d$ core-level spectra are shown in Figs. 4(e) and (f) for films grown on NGO(100) and MgO(100) substrates, respectively. The comparison of the observed peak position of the spin-orbit splitted components (Nb $3d_{5/2}$ at 206.1 eV and Nb $3d_{3/2}$ at 208.9 eV) with the reported values in the literature indicate the presence of the Nb predominantly in 4+ valence state for both the samples [53, 54]. The presence of Nb in tetravalent state indicate the strong possibility of the oxygen deficiency in the thin film samples as compared to the bulk $\text{Sr}_2\text{CoNbO}_6$, where our recent XAS measurements indicate the presence of Nb purely in the pentavalent state [26]. These oxygen deficiencies are expected to play a key role in governing the underlined transport properties of these samples, as discussed below.

Furthermore, the Co $2p$ core level XPS spectra are measured to understand the effect of the substrate induced strain and possible oxygen non-stoichiometry on the chemical environment of Co, as shown in Figs. 4(g) and (h) for the films grown on NGO(100) and MgO(100) substrates, respectively. We observe a clear splitting in the main peaks for both the $2p_{1/2}$ and $2p_{3/2}$ components, indicating the presence of the two different valence states of Co in both the samples. Further, the deconvolution of the spectra reveal the presence of an additional component, as evident from the asymmetry in the main peaks towards the higher binding energy in Figs. 4(g) and (h). The position of these three components are presented in the Table I, which resembles well with the reported values for Co^{2+} , Co^{3+} , and Co^{4+} [55, 57, 58]. This deviation in the valence states of Co in the thin films (from the 3+ state in the bulk $\text{Sr}_2\text{CoNbO}_6$ [26]) further indicate the possibility of strain induced oxygen non-stoichiometry in both the samples. Interestingly, the ratio of Co^{2+} to Co^{4+} is higher (0.61) in case of the film grown on NGO(100) substrate as compared to that (0.47) on MgO(100). An asymmetric in-plane compressive strain in case of NGO(100) substrate results in the elongation in the out-of-plane lattice parameter of $\text{Sr}_2\text{CoNbO}_6$, which possibly stabilize the Co^{2+} in the system due to its larger ionic radii as compared to Co^{3+} [59]. This small change in the fraction of the Co^{2+} with respect

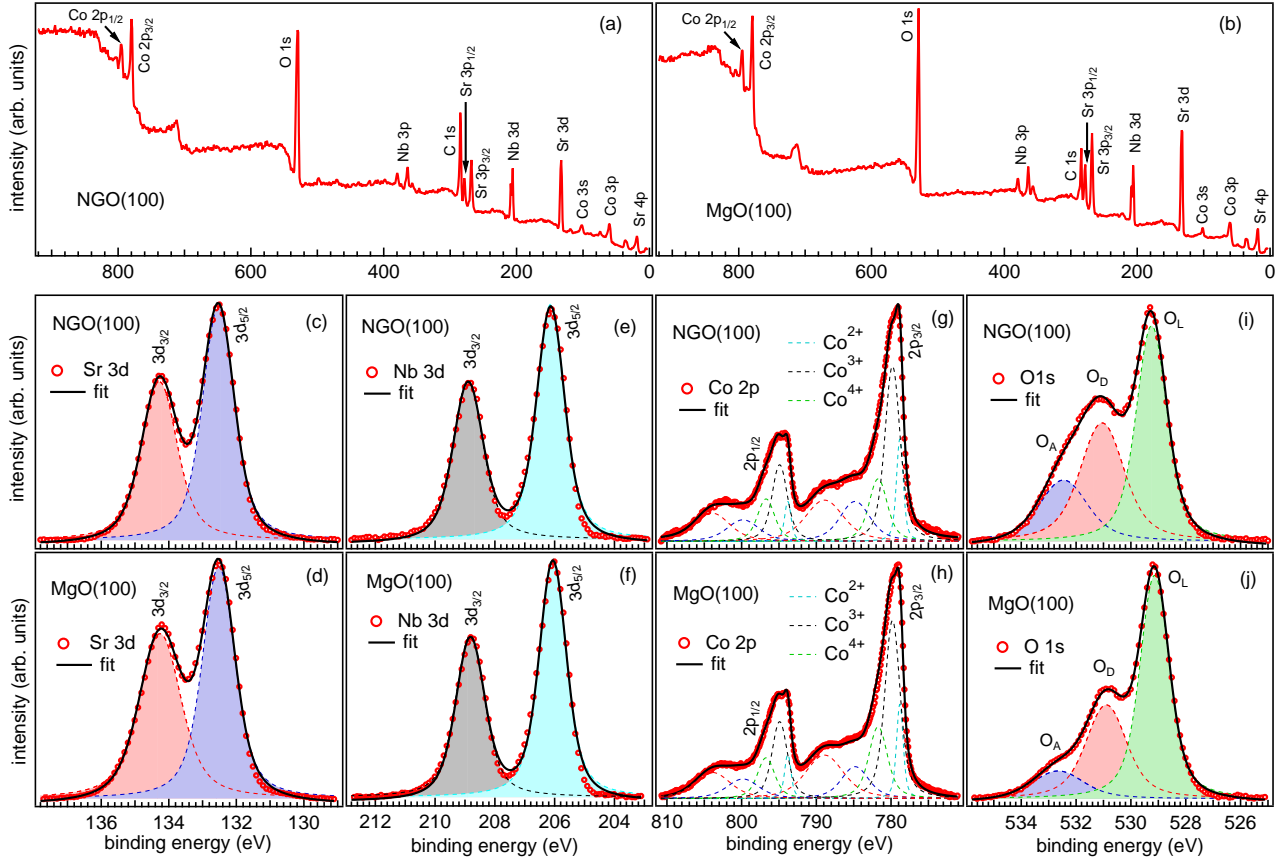


FIG. 4. (a, b) The XPS survey spectra, (c, d) Sr $3d$ core-level, (e, f) Nb $3d$ core-level, (g, h) Co $2p$ core-level, and (i, j) O $1s$ core-level spectra of the $\text{Sr}_2\text{CoNbO}_6$ thin films grown on NGO(100) and MgO(100) substrates, respectively.

to Co^{4+} with the growth orientation may also result from the fitting procedure due to the over parameterization resulting from the several components present in these samples. However, the oxygen $1s$ core-level XPS spectra discussed below clearly validate this point, which show the higher oxygen deficiencies in case of the film grown on the NGO(100) substrate as compared to MgO(100) substrate. Here, it is important to note that Co^{2+} is insulating in nature due to the lowest possible oxidation state of Co, which significantly suppress the conduction channels in the sample [38]. This results in the lower electronic conductivity of the film grown on the NGO(100) substrate as compared to that on MgO(100) substrate, as evident from the ρ - T measurements, presented in Fig. 2(a). Further, we observe the two broad satellite features around 784.8 eV and 788.9 eV which can be assigned to the Co^{2+} and Co^{3+} states, respectively [55]. Here, it is well known that Co^{2+} shows much stronger satellite feature as compared to Co^{3+} ; however, significantly large fraction of the Co^{3+} as compared to Co^{2+} in the present case results in the comparable strength of the satellite features for both the states.

Moreover, we measured the O $1s$ core-level XPS spectra to estimate the possible oxygen defects in these sam-

ples, as presented in Figs. 4(i, j). We find three well-resolved components for both the samples; however, two features at the higher BE are more clearly distinguishable in the case of film grown on MgO(100) substrate. Here, the first component around 529.1(1) eV (O_L) is attributed to the lattice oxygen in the Co/Nb–O octahedra, whereas third component around 532.6(2) (O_A) is resulting from the chemisorbed oxygen atoms, i.e., surface contamination by organic molecules [56]. Importantly, the central component around 531.0(1) (O_D) results either from the oxygen atoms with the formal charge less than $-2e$ due to the covalent character of the Co/Nb–O bonds [60, 61] or presence of oxygen deficiencies in the samples [62–64]. The intensity of this central component with respect to the lattice oxygen is much higher in case of NGO(100) film as compared to the MgO(100) [see Figs. 4(i, j)], which clearly indicate the higher oxygen deficiencies in the former. The integrated area ratio of O_D and O_L , which can be used as the measure of the oxygen deficiencies in the thin film samples [62, 63], is found to be 0.78 in case of NGO(100) substrate and 0.59 for the film grown on MgO(100) substrate. This higher oxygen deficiency in the film grown on NGO(100) substrate results in the larger concentration of Co^{2+} ions and hence lower

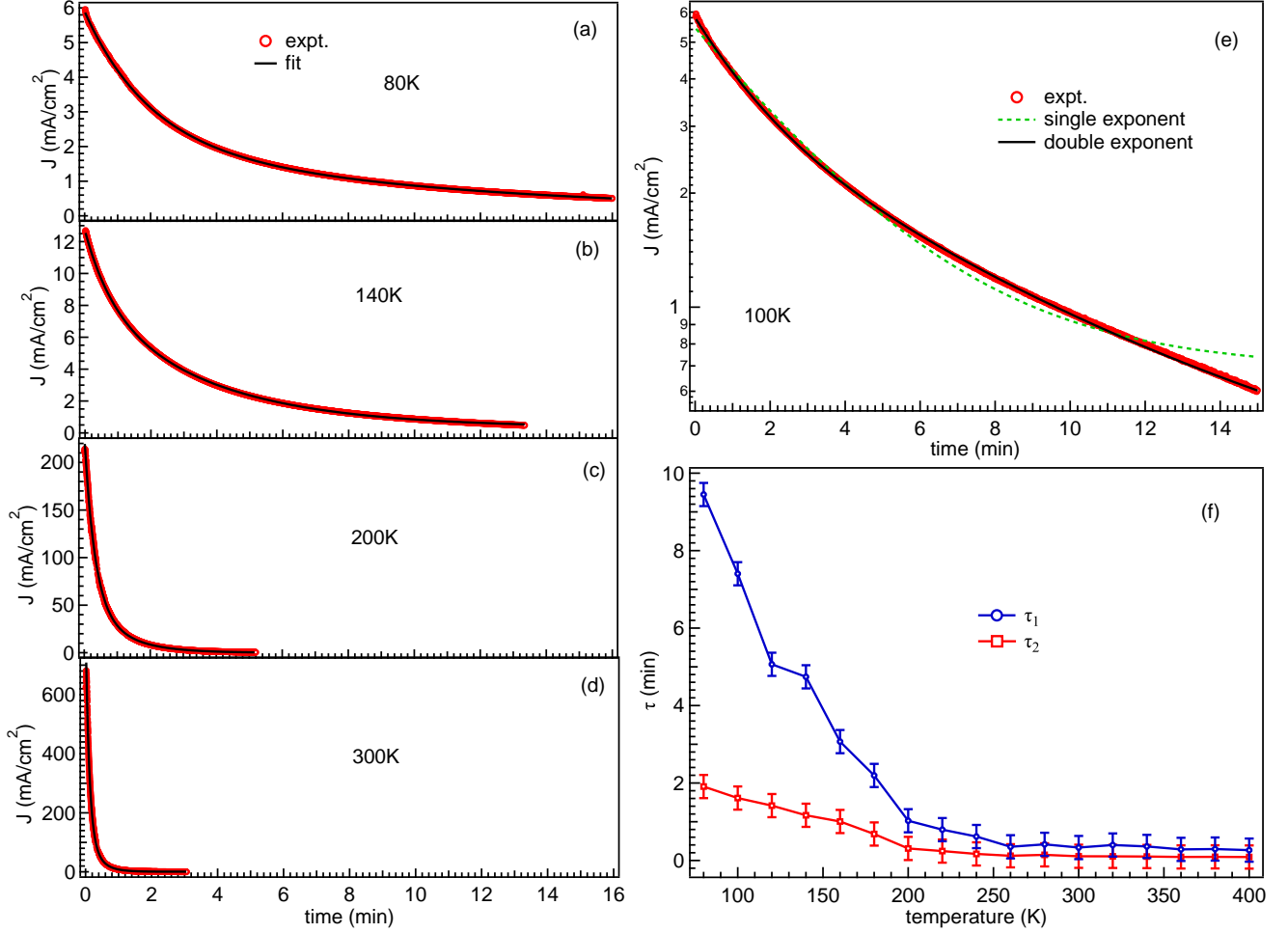


FIG. 5. (a–d) The time dependence of the current density after applying a step voltage of 500 V/cm for 3 minutes on the $\text{Sr}_2\text{CoNbO}_6/\text{NGO}(100)$ sample at the selected temperatures. (e) Fitting of the $J-t$ curve at 100 K using single (green dashed curve) and double (solid black line) exponent models (see text for more details). (f) Temperature evolution of the relaxation times for both the relaxation processes.

electronic conductivity as compared to the film grown on MgO(100) substrate, which is also evident from the Co $2p$ core-level spectra, as discussed above. However, the exact quantification of oxygen vacancies using the high end techniques such as aberration corrected transmission electron microscopy (TEM) and/or positron annihilation can give much deeper insight into their role in governing the conduction mechanism of these samples [65, 66].

Interestingly, the colossal dielectric properties observed in $\text{Sr}_2\text{CoNbO}_6$ [36] indicate its possible use in the energy storage devices, where the study of the leakage current is important to find its practical usefulness [41]. Thus, in order to estimate that, we apply a step voltage of 500 V/cm on $\text{Sr}_2\text{CoNbO}_6/\text{NGO}(100)$ sample for 3 minutes and then record the current response as a function of time (until current drops to 1 nA), as shown in Figs. 5(a–d) at some representative temperatures. Interestingly, the current persists up to several minutes at the lower temperatures and decay more rapidly with increase in

the temperature. This non-linear response of current is fitted with the sum exponent model defined as [43]

$$J(t) = \sum_{i=1}^n J_{mi} e^{-t/\tau_i} + J_0, \quad (3)$$

where J_{mi} , τ_i , and J_0 represent the initial current density, relaxation time, and steady-state current density, respectively and the summation is over the different relaxation processes. First, we try to fit the $J-t$ curves using the single exponent model. However, a significant deviation from the experimental data has been observed, as shown by the green dashed line in Fig. 5(e) for 100 K. Thus, two exponent mode with different relaxation times is used for the fitting and a nice agreement between the experimental and fitted curves can be seen, as represented by the solid black line in Fig. 5(e). This indicates the presence of two different relaxation mechanisms in the sample. Therefore, all the $J-t$ curves at different temperatures

TABLE I. The fitting parameters of the Co $2p$ ($2p_{3/2}$) and O $1s$ core-level spectra of $\text{Sr}_2\text{CoNbO}_6$ films deposited on the NGO(100) and MgO(100) substrates.

Substrate (100)	Peak	Position (eV)	FWHM (eV)	Area
Co $2p$				
NGO	2+	778.8	1.1	0.62
	3+	779.8	2.4	2.36
	4+	781.7	2.9	1.01
MgO	2+	778.8	1.1	0.56
	3+	779.8	2.4	2.40
	4+	781.7	2.9	1.18
O $1s$				
NGO	O_L	529.2	1.3	1.61
	O_D	531.0	1.9	1.26
	O_A	532.5	2.1	0.71
MgO	O_L	529.1	1.3	1.58
	O_D	530.9	1.8	0.93
	O_A	532.6	2.2	0.34

are fitted using the two exponent model and the temperature evolution of the two relaxations times is presented in Fig. 5(f). It is interesting to note that the relaxation time τ_1 is 5-6 times higher than τ_2 , which indicate significantly different origin of the two processes. The similar behavior of the $J - t$ curves with two relaxation processes has been also observed in the polycrystalline films of $\text{Pb}(\text{Zr}_{0.48}\text{Ti}_{0.52})\text{O}_3$, which are speculated to originate from the bulk and grain boundaries/sample-electrode interface [43, 67]. The effect of grain boundaries is expected to be negligible on the single crystalline film and the two relaxation processes are most likely originate from the sample and interfacial polarization in the present case. However, further investigations of the defects, twinning in the film, oxygen vacancies, carrier hopping, traps filling, etc., can shed light on the nature of these relaxation processes [68–71]. Moreover, both the relaxation times decreases with increase in the temperature up to around 200 K and then attain a very small value (< 1 min) at the higher temperatures. This is due to the enhancement in the electronic conductivity and hence availability of the more charge carriers at the higher temperature. Thus, a large dielectric constant observed in $\text{Sr}_2\text{CoNbO}_6$ near the room temperature [36] is possible accompanied with the higher electronic conductivity in the sample, which limit its practical use in the charge storage applications and hence further engineering of the electronic band gap is required for its practical use.

Finally, we show the Raman spectra for the films grown on NGO(100) and MgO(100) substrates, in Figs. 6(a, b), respectively. We observe several Raman active modes between $380\text{--}770\text{cm}^{-1}$ for both the samples, unlike bulk $\text{Sr}_2\text{CoNbO}_6$ which shows only two very weak Raman modes [38]. This suggest the reduction in the crystal

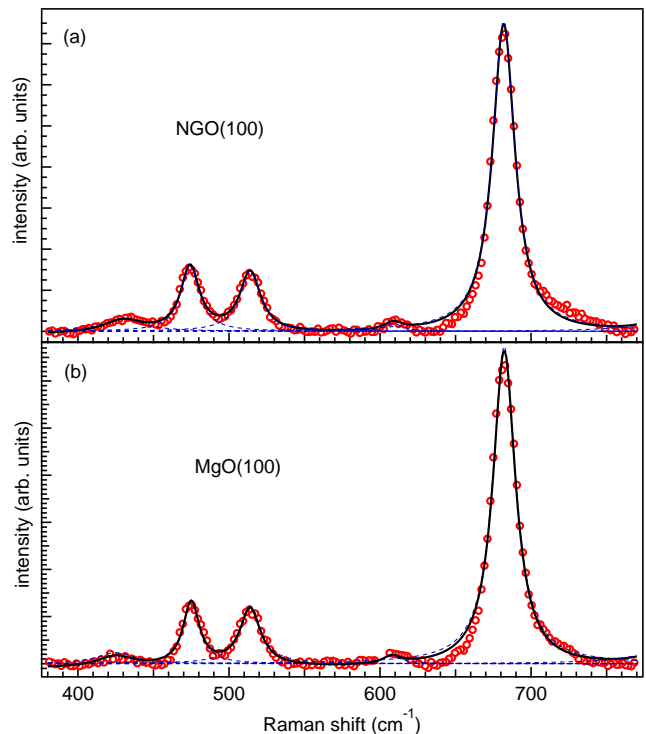


FIG. 6. The room temperature Raman spectra of $\text{Sr}_2\text{CoNbO}_6$ thin films grown on (a) NGO(100) and (b) MgO(100) substrates using the 514.5 nm excitation wavelength.

symmetry in the thin film samples as compared to the bulk $\text{Sr}_2\text{CoNbO}_6$ possibly due to the distortion in the (Co/Nb) O_6 octahedra resulting from the substrate induced strain. For example, the presence of the three Raman modes between $400\text{--}550\text{cm}^{-1}$ represent the oxygen bending modes in the $P2_1/n$ (monoclinic) symmetry, as no Raman active modes are expected at this wave number for the $I4/m$ (tetragonal) space group of the bulk $\text{Sr}_2\text{CoNbO}_6$ material [20, 38, 72]. Note that the lowering in the crystal symmetry in the double perovskite oxides is usually accompanied with the enhancement in the B-site ordering. Thus, the presence of these Raman active modes suggests the growth of B-site ordered thin films from the almost disordered bulk $\text{Sr}_2\text{CoNbO}_6$ sample [26, 38]. This is consistent as the substrate induced strain is considered an effective way to grow the ordered thin films from the disordered target materials [29, 73–75]. However, no significant change is observed in the Raman spectra for both the sample, which indicate that any change in the degree of the octahedral distortion and/or B-site ordering due to change in the growth orientation can not be probed using the unpolarized Raman spectroscopy in the present case and the polarization dependent Raman spectra can be more useful [28].

IV. CONCLUSIONS

The oxygen stoichiometry and hence the resulting electronic and transport properties of $\text{Sr}_2\text{CoNbO}_6$ have been engineered with change in the growth orientation of the epitaxial thin films using pulsed laser deposition. The films of $\text{Sr}_2\text{CoNbO}_6$ have been grown along a and c -axis on orthorhombic NGO(100) and cubic MgO(100) substrates, resulting in the asymmetric compressive and symmetric tensile in-plane strain, respectively. The film grown on the NGO(100) substrate have the higher degree of the oxygen deficiency, which results in the larger fraction of Co in 2+ valence state and hence derive the system toward the insulating regime as compared to that grown on MgO(100) substrate. The XPS measurements shows the presence of Co in the 2+, 3+ as well as 4+ valence states, resulting from the in-plane compressive (tensile) and hence out-of-plane tensile (compressive) strain in case of the film grown on the NGO(100) [MgO(100)] substrate. Moreover, the divalent and tetravalent states of Sr and Nb, respectively, are found to remain invariant with the growth orientation in the two cases. Interestingly, the investigation of the leakage current indicate that the colossal dielectric properties observed in bulk

$\text{Sr}_2\text{CoNbO}_6$ near room temperature originate from the higher electronic conductivity in the sample. Moreover, the Raman spectra evident the significant reduction in the crystal symmetry in the thin films as compared to the bulk $\text{Sr}_2\text{CoNbO}_6$.

V. ACKNOWLEDGMENT

AK acknowledges the UGC India for fellowship and the physics department of IIT Delhi for providing the the XRD, AFM, and PPMS EVERCOOL facilities, and central research facilities (CRF) of IIT Delhi for providing the Raman spectrometer. AK thanks Rishabh Shukla for his help during the thin film deposition. AK also thanks Ploybussara Gomasang for help in the XPS measurements at the Shibaura Institute of Technology, Japan, which were supported by Sakura Science Program (aPBL). RM thanks IUAC for providing the experimental facilities. The PLD instrument used for thin film growth is financially supported by IIT Delhi through seed grant with Reference No. BPHY2368 and SERB-DST through early career research (ECR) award with Project Reference No. ECR/2015/000159. RSD also acknowledges the SERB-DST for financial support through a core research grant (project reference no. CRG/2020/003436).

-
- [1] J. Pérez, J. García, J. Blasco, and J. Stankiewicz, Spin-Glass Behavior and Giant Magnetoresistance in the (RE) $\text{Ni}_{0.3}\text{Co}_{0.7}\text{O}_3$ (RE=La, Nd, Sm) System, *Phys. Rev. Lett.* **80**, 2401 (1998).
 - [2] A. K. Kundu, P. Nordblad, and C. N. R. Rao, Nonequilibrium magnetic properties of single-crystalline $\text{La}_{0.7}\text{Ca}_{0.3}\text{CoO}_3$, *Phys. Rev. B* **72**, 144423 (2005).
 - [3] Rishabh Shukla and R. S. Dhaka, Anomalous magnetic and spin glass behavior in Nb substituted $\text{LaCo}_{1-x}\text{Nb}_x\text{O}_3$, *Phys. Rev. B* **97**, 024430 (2018).
 - [4] Rishabh Shukla, and R. S. Dhaka, Evolution of complex magnetic phases and metal-insulator transition through Nb substitution in $\text{La}_{0.5}\text{Sr}_{0.5}\text{Co}_{1-x}\text{Nb}_x\text{O}_3$, *Phys. Rev. B* **107**, 165108 (2023).
 - [5] G. Giovannetti, S. Kumar, D. Khomskii, S. Picozzi, and J. V. D. Brink, Multiferroicity in Rare-Earth Nickelates RNiO_3 , *Phys. Rev. Lett.* **103**, 156401 (2009).
 - [6] Z. G. Sheng, J. Gao, and Y. P. Sun, Current-induced resistive switching effect in oxygen-deficient $\text{La}_{0.8}\text{Ca}_{0.2}\text{MnO}_{3-\delta}$ films, *Phys. Rev. B* **79**, 014433 (2009).
 - [7] S. Tao and J. T. S. Irvine, A redox-stable efficient anode for solid-oxide fuel cells, *Nat. Mater.* **2**, 320 (2003).
 - [8] J. Chakrabartty, C. Harnagea, M. Celikin, F. Rosei, and R. Nechache, Improved photovoltaic performance from inorganic perovskite oxide thin films with mixed crystal phases, *Nat. Photonics.* **12**, 271 (2018).
 - [9] M. Das, S. Roy, and P. Mandal, Giant reversible magnetocaloric effect in a multiferroic GdFeO_3 single crystal, *Phys. Rev. B* **96**, 174405 (2017).
 - [10] J.-M. Chen, Y.-Y. Chin, M. Valldor, Z. Hu, J.-M. Lee, S.-C. Haw, N. Hiraoka, H. Ishii, C.-W. Pao, K.-D. Tsuei, J.-F. Lee, H.-J. Lin, L.-Y. Jang, A. Tanaka, C.-T. Chen, and L. H. Tjeng, A Complete High-to-Low spin state Transition of Trivalent Cobalt Ion in Octahedral Symmetry in $\text{SrCo}_{0.5}\text{Ru}_{0.5}\text{O}_{3-\delta}$, *J. Am. Chem. Soc.* **136**, 1514 (2014).
 - [11] T. Saitoh, T. Mizokawa, A. Fujimori, M. Abbate, Y. Takeda, and M. Takano, Electronic structure and temperature-induced paramagnetism in LaCoO_3 , *Phys. Rev. B* **55**, 4257 (1997).
 - [12] Hemanshu Dua, Rishabh Shukla, and R. S. Dhaka, Structural phase transition and its consequences on optical behavior of $\text{LaV}_{1-x}\text{Nb}_x\text{O}_4$, *Phys. Rev. B* **103**, 174107 (2021).
 - [13] A. Deb, J. M. Ralph, E. J. Cairnsand, and U. Bergmann, Characterization of $\text{La}_{0.8}\text{Sr}_{0.2}\text{FeO}_{3-\delta}$ and $\text{La}_{0.7}\text{Sr}_{0.2}\text{FeO}_{3-\delta}$ as a function of temperature by x-ray absorption spectroscopy, *Phys. Rev. B* **73**, 115114 (2006).
 - [14] C. R. Sankar and P. A. Joy, Magnetic properties of the self-doped lanthanum manganites $\text{La}_{1-x}\text{MnO}_3$, *Phys. Rev. B* **72**, 024405 (2005).
 - [15] A. Ohtomo and H. Y. Hwang, A high-mobility electron gas at the $\text{LaAlO}_3/\text{SrTiO}_3$ heterointerface, *Nature* **427**, 423 (2004).
 - [16] D. Fuchs, C. Pinta, T. Schwarz, P. Schweiss, P. Nagel, S. Schuppler, R. Schneider, M. Merz, G. Roth, and H. V. Löhneysen, Ferromagnetic order in epitaxially strained LaCoO_3 thin films, *Phys. Rev. B* **75**, 144402 (2007).
 - [17] J. R. Petrie, C. Mitra, H. Jeen, W. S. Choi, T. L. Meyer, F. A. Reboredo, J. W. Freeland, G. Eres, and H. N. Lee,

- Strain control of oxygen vacancies in epitaxial strontium cobaltite films, *Avd. Funct. Mater.* **26**, 1564 (2016).
- [18] A. Herklotz, D. Lee, E.-J. Guo, T. L. Meyer, J. R. Petrie, and H. N. Lee, Strain coupling of oxygen non-stoichiometry in perovskite thin films, *J. Phys.: Condens. Matter* **29**, 493001 (2017).
- [19] U. Aschauer, R. Pfenninger, S. M. Selbach, T. Grande, and N. A. Spaldin, Strain-controlled oxygen vacancy formation and ordering in CaMnO_3 , *Phys. Rev. B* **88**, 054111 (2013).
- [20] Ajay Kumar, R. Shukla, A. Pandey, S. Dalal, M. Miryala, K. Ueno, M. Murakami, and R. S. Dhaka, Structural, transport, optical, and electronic properties of $\text{Sr}_2\text{CoNbO}_6$ thin films, *J. Appl. Phys.* **128**, 025303 (2020).
- [21] S. Esser, C. F. Chang, C.-Y. Kuo, S. Merten, V. Roddatis, T. D. Ha, A. Jesche, V. Moshnyaga, H.-J. Lin, A. Tanaka, C. T. Chen, L. H. Tjeng, and P. Gegenwart, Strain-induced changes of the electronic properties of B-site ordered double-perovskite $\text{Sr}_2\text{CoIrO}_6$ thin films, *Phys. Rev. B* **97** 205121 (2018).
- [22] D. Niebieskikwiat, F. Prado, A. Caneiro, and R. D. Sánchez, Antisite defects versus grain boundary competition in the tunneling magnetoresistance of $\text{Sr}_2\text{FeMoO}_6$ double perovskite, *Phys. Rev. B* **70**, 132412 (2004).
- [23] D. Sánchez, J. A. Alonso, M. García-Hernández, M. J. Martínez-Lope, J. L. Martínez, and A. Mellergård, Origin of neutron magnetic scattering in antisite-disordered $\text{Sr}_2\text{FeMoO}_6$ double perovskites, *Phys. Rev. B* **65**, 104426 (2002).
- [24] A. Jung, I. Bonn, V. Ksenofontov, M. Panthöfer, S. Reiman, C. Felser, and W. Tremel, Effect of cation disorder on the magnetic properties of $\text{Sr}_2\text{Fe}_{1-x}\text{GaxReO}_6$ ($0 < x < 0.7$) double perovskites, *Phys. Rev. B* **75**, 184409 (2007).
- [25] Ajay Kumar, A. Jain, S. M. Yusuf, and R. S. Dhaka, Observation of Anisotropic Thermal Expansion and the Jahn-Teller Effect in Double Perovskites $\text{Sr}_{2-x}\text{La}_x\text{CoNbO}_6$ Using Neutron Diffraction, *J. Phys. Chem. Lett.* **13**, 3023 (2022).
- [26] Ajay Kumar, R. Shukla, R. Kumar, R. J. Choudhary, S. N. Jha, and R. S. Dhaka, Probing the electronic and local structure of $\text{Sr}_{2-x}\text{La}_x\text{CoNbO}_6$ using near-edge and extended x-ray absorption fine structures, *Phys. Rev. B* **105**, 245155 (2022).
- [27] A. Vailionis, H. Boschker, W. Siemons, E. P. Houwman, D. H. A. Blank, G. Rijnders, and G. Koster, Misfit strain accommodation in epitaxial ABO_3 perovskites: Lattice rotations and lattice modulations, *Phys. Rev. B* **83**, 064101 (2011).
- [28] M. N. Iliev, M. V. Abrashev, A. P. Litvinchuk, V. G. Hadjiev, H. Guo, and A. Gupta, Raman spectroscopy of ordered double perovskite $\text{La}_2\text{CoMnO}_6$ thin films, *Phys. Rev. B* **75**, 104118 (2007).
- [29] J. E. Kleibecker, E. M. Choi, E. D. Jones, T.-M. Yu, B. Sala, B. A. MacLaren, D. Kepaptsoglou, D. H. Maldonado, Q. M. Ramasse, L. Jones, J. Barthel, I. MacLaren, and J. L. M. Driscoll, Route to achieving perfect B-site ordering in double perovskite thin films, *NPG Asia Mater.* **9**, e406 (2017).
- [30] R. Galceran, L. L.-Mir, B. Bozzo, J. C.-Fernández, J. Santiso, L. Balcells, C. Frontera, and B. Martínez, Strain-induced perpendicular magnetic anisotropy in $\text{La}_2\text{CoMnO}_{6-\epsilon}$ thin films and its dependence on film thickness, *Phys. Rev. B* **93**, 144417 (2016).
- [31] S. J. Callori, S. Hu, J. Bertinshaw, Z. J. Yue, S. Danilkin, X. L. Wang, V. Nagarajan, F. Klöse, J. Seidel, and C. Ulrich, Strain-induced magnetic phase transition in $\text{SrCoO}_{3-\delta}$ thin films, *Phys. Rev. B* **91**, 140405(R) (2015).
- [32] Rishabh Shukla, Ajay Kumar, Sandeep Dalal, Akhilesh Pandey, and R. S. Dhaka, Structural and transport properties of $\text{La}_{1-x}\text{Sr}_x\text{Co}_{1-y}\text{Nb}_y\text{O}_3$ epitaxial thin films, *Thin Solid Films*, 709, 138250 (2020).
- [33] G. King and P. M. Woodward, Cation ordering in perovskites, *J. Mater. Chem.* **20**, 5785 (2010).
- [34] S. Vasala and M. Karppinen, $\text{A}_2\text{B}'\text{B}''\text{O}_6$ perovskites: A review, *Prog. in solid st. Chem.* **43**, 1 (2015).
- [35] S. Xu, X. Lin, B. Ge, D. Ai, and Z. Peng, Conducting mechanism of Sr_2CoRO_6 ($\text{R} = \text{Mo}, \text{Nb}$) under different P_{O_2} , *J. Ceram. Soc. Jpn.* **124** [8], 813 (2016).
- [36] G. J. Wang, C. C. Wang, S. G. Huang, X. H. Sun, C. M. Lei, T. Li, and L. N. Liu, Origin of the colossal dielectric properties in double-perovskite $\text{Sr}_2\text{CoNbO}_6$, *AIP adv.* **3**, 022109 (2013).
- [37] J. Bashir and R. Shaheen, Structural and complex AC impedance spectroscopic studies of A_2CoNbO_6 ($\text{A}=\text{Sr}, \text{Ba}$) ordered double perovskites, *Solid State Sci.* **13**, 993 (2011).
- [38] Ajay Kumar and R. S. Dhaka, Unraveling magnetic interactions and the spin state in insulating $\text{Sr}_{2-x}\text{La}_x\text{CoNbO}_6$, *Phys. Rev. B* **101**, 094434 (2020).
- [39] Ajay Kumar, B. Schwarz, H. Ehrenberg, and R. S. Dhaka, Evidence of discrete energy states and cluster-glass behavior in $\text{Sr}_{2-x}\text{La}_x\text{CoNbO}_6$, *Phys. Rev. B* **102**, 184414 (2020).
- [40] D. He, X. Du, H. Mei, Y. Zhong and N. Cheng, Electronic structure and physical properties of double perovskite A_2CoNbO_6 ($\text{A}=\text{Sr}, \text{Ba}$) crystals, *J. Phys.: Condens. Matter* **32**, 135702 (2020).
- [41] B. Nagaraj, S. Aggarwal, T. K. Song, T. Sawhney, and R. Ramesh, Leakage current mechanisms in lead-based thin-film ferroelectric capacitors, *Phys. Rev. B* **59**, 16022 (1999).
- [42] C. Zhang, Z. Zeng, Z. Zhu, M. Karami, and X. Chen, Impact of Leakage for Electricity Generation by Pyroelectric Converters, *Phys. Rev. Appl.* **14**, 064079 (2020).
- [43] Y. Podgorny, K. Vorotilov, and A. Sigov, Estimation of steady-state leakage current in polycrystalline PZT thin films, *AIP Adv.* **6**, 095025 (2016).
- [44] H. Boschker, M. Mathews, E. P. Houwman, H. Nishikawa, A. Vailionis, G. Koster, G. Rijnders, and D. H. A. Blank, Strong uniaxial in-plane magnetic anisotropy of (001)- and (011)-oriented $\text{La}_{0.67}\text{Sr}_{0.33}\text{MnO}_3$ thin films on NdGaO_3 substrates, *Phys. Rev. B* **79**, 214425 (2009).
- [45] Z. Huang, L. F. Wang, P. F. Chen, G. Y. Gao, X. L. Tan, B. W. Zhi, X. F. Xuan, and W. B. Wu, Tuning the ground state of $\text{La}_{0.67}\text{Ca}_{0.33}\text{MnO}_3$ films via coherent growth on orthorhombic NdGaO_3 substrates with different orientations, *Phys. Rev. B* **86**, 014410 (2012).
- [46] T. H. Kim, T. R. Paudel, R. J. Green, K. Song, H.-S. Lee, S.-Y. Choi, J. Irwin, B. Noesges, L. J. Brillson, M. S. Rzchowski, G. A. Sawatzky, E. Y. Tsymbal, and C. B. Eom, Strain-driven disproportionation at a correlated oxide metal-insulator transition, *Phys. Rev. B* **101**, 121105(R) (2020).
- [47] M. Tyunina, O. Pacherova, T. Kocourek, and A. Dejneka, Anisotropic chemical expansion due to oxygen vacancies in perovskite films, *Sci. Rep.* **11**, 15247 (2021).

- [48] J. Nichols, J. Terzic, E. G. Bittle, O. B. Korneta, L. E. De Long, J. W. Brill, G. Cao, and S. S. A. Seo, Tuning electronic structure via epitaxial strain in Sr_2IrO_4 thin films, *Appl. Phys. Lett.* **102**, 141908 (2013).
- [49] T. Huang, Y. Wang, H. Li, M. Wang, Y. Lyu, S. Shen, N. Lu, Q. He, and P. Yu, Tuning the electronic properties of epitaxial strained $\text{CaFeO}_{3-\delta}$ thin films, *Appl. Phys. Lett.* **114**, 221907 (2019).
- [50] R. P. Vasquez, X-ray photoelectron spectroscopy study of Sr and Ba compounds, *J. Electron Spectrosc.* **56**, 217 (1991).
- [51] R. S. Dhaka, S. W. D'Souza, M. Maniraj, A. Chakrabarti, D. L. Schlagel, T. A. Lograsso, and S. R. Barman, Photoemission study of the (100) surface of Ni_2MnGa and Mn_2NiGa ferromagnetic shape memory alloys, *Surface Science*, **603**, 1999 (2009).
- [52] M. I. Sosulnikov and Y. A. Tetrin, X-ray photoelectron studies of Ca, Sr and Ba and their oxides and carbonates, *J. Electron Spectrosc.* **59**, 111 (1992).
- [53] M. K. Bahl, ESCA studies of some niobium compounds, *J. Phys. Chem. Solids* **36**, 485 (1975).
- [54] F. J. Wong, N. Hong, and S. Ramanathan, Orbital splitting and optical conductivity of the insulating state of NbO_2 , *Phys. Rev. B* **90**, 115135 (2014).
- [55] T. J. Chung, C. R. Brundle, and D. W. Rice, Interpretation of the X-ray photoemission spectra of cobalt oxide and cobalt oxide surfaces, *Surf. Sci.* **59**, 413 (1976).
- [56] Rishabh Shukla, Clemens Ulrich, and R. S. Dhaka, Investigation of lattice dynamics, magnetism and electronic transport in $\beta\text{-Na}_{0.33}\text{V}_2\text{O}_5$, *Phys. Rev. B* **106**, 125148 (2022).
- [57] M. C. Biesinger, B. P. Payne, A. P. Grosvenor, L. W. M. Lau, A. R. Gerson, R. S. C. Smart, Resolving surface chemical states in XPS analysis of first row transition metals, oxides and hydroxides: Cr, Mn, Fe, Co and Ni, *Appl. Surf. Sci.* **257**, 2717 (2011).
- [58] J. C. Dupin, D. Gonbeau, H. B.-Moudden, P. Vinatier, and A. Levasseur, XPS analysis of new lithium cobalt oxide thin-films before and after lithium deintercalation, *Thin Solid Films* **384**, 23 (2001).
- [59] R. D. Shannon, Revised effective ionic radii and systematic studies of interatomic distances in halides and chalcogenides, *Acta Cryst.* **A32**, 751 (1976).
- [60] J.-C. Dupin, D. Gonbeau, P. Vinatier, and A. Levasseur, Systematic XPS studies of metal oxides, hydroxides and peroxides, *Phys. Chem. Chem. Phys.* **2**, 1319 (2000).
- [61] L. Q. Wu, Y. C. Li, S. Q. Li, Z. Z. Li, G. D. Tang, W. H. Qi, L. C. Xue, X. S. Ge, and L. L. Ding, Method of estimating ionicities of oxides using O1s photoelectron spectra, *AIP Adv.* **5**, 097210 (2015).
- [62] J. Cui, Y. Zhang, J. Wang, Z. Zhao, H. Huang, W. Zou, M. Yang, R. Peng, W. Yan, Q. Huang, Z. Fu, and Y. Lu, Oxygen deficiency induced strong electron localization in lanthanum doped transparent perovskite oxide BaSnO_3 , *Phys. Rev. B* **100**, 165312 (2019).
- [63] H. J. Cho, B. Feng, T. Onozato, M. Wei, A. V. Sanchela, Y. Ikuhara, and H. Ohta, Investigation of electrical and thermal transport property reductions in La-doped BaSnO_3 films, *Phys. Rev. Mater.* **3**, 094601 (2019).
- [64] F. Lei, Y. Sun, K. Liu, S. Gao, L. Liang, B. Pan, and Y. Xie, Oxygen vacancies confined in ultrathin Indium Oxide porous sheets for promoted visible-light water splitting, *J. Am. Chem. Soc.* **136**, 6826 (2014).
- [65] N. Gauquelin, K. H. W. van den Bos, A. B  ch  , F. F. Krause, I. Lobato, S. Lazar, A. Rosenauer, S. Van Aert, and J. Verbeeck, Determining oxygen relaxations at an interface: A comparative study between transmission electron microscopy techniques, *Ultramicroscopy* **181**, 178 (2017).
- [66] M. Reiner, T. Gigl, R. Jany, G. Hammerl, and C. Hugschmidt, Detection and imaging of the oxygen deficiency in single crystalline $\text{YBa}_2\text{Cu}_3\text{O}_{7-\delta}$ thin films using a scanning positron beam, *Appl. Phys. Lett.* **106**, 111910 (2015).
- [67] Yu. V. Podgorny, D. S. Seregin, A. S. Sigov, and K. A. Vorotilov, Depolarization currents in thin ferroelectric films, *Ferroelectrics* **439**, 56 (2012).
- [68] I. Stolichnov and A. Tagantsev, Space-charge influenced-injection model for conduction in $\text{Pb}(\text{Zr}_x\text{Ti}_{1-x})\text{O}_3$ thin films, *J. Appl. Phys.* **84**, 3216 (1998).
- [69] S.-G. Yoon, A. I. Kingon, and S.-H. Kim, Relaxation and leakage current characteristics of $\text{Pb}_{1-x}\text{La}_x(\text{Zr}_y\text{Ti}_{1-y})_{1-x/4}\text{O}_3$ thin films with various Ir-based top electrodes, *J. Appl. Phys.* **88**, 6690 (2000).
- [70] L. Pintilie, I. Vrejoiu, D. Hesse, G. LeRhun, and M. Alexe, Ferroelectric polarization-leakage current relation in high quality epitaxial $\text{Pb}(\text{Zr,Ti})\text{O}_3$ films, *Phys. Rev. B* **75**, 104103 (2007).
- [71] T. Rojac, S. Drnovsek, A. Bencan, B. Malic, and D. Damjanovic, Role of charged defects on the electrical and electromechanical properties of rhombohedral $\text{Pb}(\text{Zr,Ti})\text{O}_3$ with oxygen octahedra tilts, *Phys. Rev. B* **93**, 014102 (2016).
- [72] R. L. Andrews, A. M. Heyns, and P. M. Woodward, Raman studies of A_2MWO_6 tungstate double perovskites, *Dalton Trans.* **44**, 10700 (2015).
- [73] S. Chakraverty, X. Z. Yu, M. Kawasaki, Y. Tokura, and H. Y. Hwang, Spontaneous B-site order and metallic ferrimagnetism in LaSrVMoO_6 grown by pulsed laser deposition, *Appl. Phys. Lett.* **102**, 222406 (2013).
- [74] S. Chakraverty, A. Ohtomo, D. Okuyama, M. Saito, M. Okude R. Kumai, T. Arima, Y. Tokura, S. Tsukimoto, Y. Ikuhara, and M. Kawasaki, Ferrimagnetism and spontaneous ordering of transition metals in double perovskite $\text{La}_2\text{CrFeO}_6$ films, *Phys. Rev. B* **84**, 064436 (2011).
- [75] K. Yoshimatsu, K. Nogami, K. Watarai, K. Horiba, H. Kumigashira, O. Sakata, T. Oshima, and A. Ohtomo, Synthesis and magnetic properties of double-perovskite oxide $\text{La}_2\text{MnFeO}_6$ thin films, *Phys. Rev. B* **91**, 054421 (2015).